ELSEVIER

Combustion and Flame 133 (2003) 241–254

Combustion and Flame

# $N_2$ CARS thermometry and $O_2$ LIF concentration measurements in a flame under electrically induced microbuoyancy

M.J. Papac[a], D. Dunn-Rankin[a,*], C.B. Stipe[b], D. Lucas[c]

[a]*Department of Mechanical and Aerospace Engineering, University of California at Irvine, Irvine, CA 92697-3975*
[b]*Department of Mechanical Engineering, University of California at Berkeley, Berkeley, CA 94720*
[c]*Environmental Energies Technology Division, Lawrence Berkeley Laboratory, Berkeley, CA 94720*

Received 22 August 2002; received in revised form 20 December 2002; accepted 24 December 2002

**Abstract**

Microgravity combustion is fundamentally characterized by the absence of buoyancy driven flows. To facilitate a large range of diagnostics on microgravity flames, it is useful to create an equivalent microbuoyant condition in an earth-based laboratory. This experiment simulates microbuoyancy using electric fields to balance local convection in a region of the flame. Previous studies used $N_2$ coherent anti-Stokes Raman spectroscopy (CARS) temperature measurements to show that a region exists in which the temperature profile corresponds to that of a spherically symmetric diffusion profile, as would be expected in a true microgravity environment. The current study utilizes CARS thermometry and laser induced fluorescence (LIF) to examine the temperature and $O_2$ concentration profiles in a region below the flame. The results show that the electrically balanced flame apparatus produces a spherically symmetric wedge of microbuoyant flame extending 10° from the vertical axis of the capillary flame arrangement; thereby quantifying the extent of the microbuoyant region. 

*Keywords:* Microgravity combustion; Electric field; Diffusion flame; Ion wind

## 1. Introduction

During recent years, experimental studies have been motivated by the need for refined theoretical models of combustion. Numerical simulations that encompass full chemically reacting flows, for example, are being used to examine intermediate chemical (kinetic) reactions. The simplification of flame geometry afforded by symmetric combustion allows for more complexity in flame chemistry and transport within current computational constraints. Experimental verification of these models, however, may not require full spherical symmetry for comparison so long as the effects are essentially radial and bounded. To this end, we look to a spherically symmetry wedge of flame that exhibits the same character as if it came from a fully spherically symmetric flame. This has been one justification for porous sphere experiments in drop towers, parabolic flights and in space. Since the feed tube to the sphere disrupts its symmetry, the assumption that the flame need only achieve symmetry over most of its surface is implicit.

During the combustion of hydrocarbon fuels, ions are generated which can be manipulated by the application of an external body force to counteract the effects of buoyancy. Since the ions are electrically

* Corresponding author. Tel.: +1-949-824-8745; fax: +1-949-824-8585.
*E-mail address:* ddunnran@uci.edu (D. Dunn-Rankin).

0010-2180/03/$ – see front matter 
doi:10.1016/S0010-2180(03)00011-7

charged, an external electric field can be applied as a convenient forcing mechanism. Due to the mobility of charge carriers in the combustion field, a body force several times that of gravity can be generated quite easily via ion wind [1]. Earlier work, accomplished by Carleton and Weinberg [2], utilized a similar apparatus to the one presented here to show that a microbuoyant condition can be achieved in this fashion. In their work, a grounded capillary was suspended over electrified wire gauze, and the voltage was increased until the point of microbuoyancy was achieved. The point of balance was observed to coincide with many visual properties. Subsequently, a second gauze plane was introduced to enhance the stability of the flame at the point of balance [3].

The use of physical probes (such as thermocouples) in these delicate flame environments disturbs the quantity being measured, and disrupts the electric field sustaining microbuoyancy. Therefore, we use optical diagnostics to provide quantitative measurements of the temperature and $O_2$ profiles in the region extending outside of the flame. Coherent anti-Stokes Raman spectroscopy (CARS) is used to probe the temperature field directly below the flame, as an extension to previous work [3]. The extent of spherical symmetry is ascertained by comparing radial temperature profiles extending from what is known as the point of balance. Laser induced fluorescence (LIF) is used to measure $O_2$ concentrations in the same region, providing further evidence of flame structure under electrically induced microbuoyancy in this region.

## 2. Basic equations

The classical analysis of droplet combustion is attributed to Spalding and Godsave [4,5], and is available in a number of combustion texts. The formulation of the equations given here is obtained from Turns [6]. The limitations of this theory due to its simplifying assumptions are well known [7], but it is important to reiterate a few for our discussion. Specifically, the important assumptions regarding spherical symmetry and quasi-steady burning lead to the elimination of transient terms in the governing equations and provide a useful relation for the combustion of a continuously fed system. The classical temperature and oxidizer profiles in the region outside of a droplet fed flame are:

$$T(r) = \frac{(T_f - T_\infty)\exp(-Z\dot{m}_f/r) + T_\infty \exp(-Z\dot{m}_f/r_f) - T_f}{\exp(-Z\dot{m}_f/r_f) - 1} \quad (1)$$

$$Y_{OX}(r) = Y_\infty \nu \left( \frac{\exp(-Z\dot{m}_f/r)}{\exp(-Z\dot{m}_f/r_f)} - 1 \right) \quad (2)$$

where $Z = C_p/4\pi k = 1/4\pi\rho D$ is the Zeldovich parameter for unity Lewis number, $\dot{m}_f$ is the mass flow rate of fuel, $C_p$ is the specific heat of the gaseous mixture, $k$ is the thermal conductivity of the gaseous mixture, $\rho$ is the density of the gaseous mixture, $D$ is the diffusion coefficient of the gaseous mixture, $r_f$ is the flame radius, and $\nu$ is the stoichiometric coefficient by mass.

The droplet equations are identical in the outer region of the flame for spherical gas combustion since the outer region depends solely on two boundary conditions corresponding to the flame front and to the infinitely distant boundary. Analysis in this region requires specific knowledge of both thermal and diffusive properties of the surrounding gas, and is typically performed by: 1) assuming unity Lewis number; and 2) by holding $\rho D$ constant during integration. The main source of discrepancy is due to the latter assumption. In fact, this term stays relatively constant between 300 to 1000K, but varies within a factor of 5 between 1000K and 2000 K for $CH_4$-air combustion. Further simplifications can be made in the case of low fuel flow rates by expanding the exponential terms to first order, resulting in the following equations that are easily fitted to experimental data.

$$T(r) = \frac{T_f r_f}{r} + T_\infty \quad (3)$$

$$Y_{OX}(r) = \frac{Z\dot{m}_f}{r_f - Z\dot{m}_f}\left(1 - \frac{r_f}{r}\right) \quad (4)$$

For conditions typical of our experiments, the error due to this approximation is less than 1.2% and 4% throughout the area of interest for temperature and oxidizer ($O_2$) concentration, respectively.

## 3. Microbuoyant capillary flame apparatus

In the experiments, a semi-spherical diffusion flame is created at the end of a stainless steel capillary, as in Figs. 1 and 2. One permeable stainless steel gauze plane is placed above the flame with the capillary tube protruding through it. Both the tube and the gauze plane are held at a high electric potential. An identical, but grounded, gauze plane is placed below the capillary so that the flame is centered between the two gauze planes. Previous work and experiments show that this upper plane stabilizes the flame near the microbuoyant condition. Flame stability becomes important when making point-wise measurements in a plane if they are to be considered

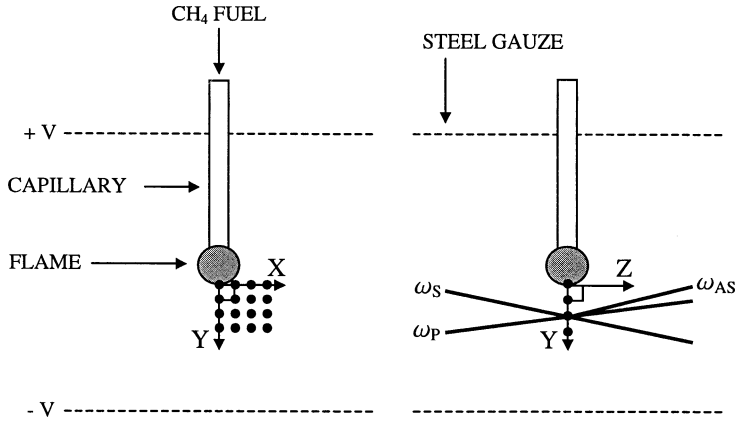


Fig. 1. Schematic of the electrically induced microbuoyant flame and measurement locations taken in the z-plane.

representative of the corresponding region. Methane fuel is injected through the 1.7 mm OD capillary via multistage pressure regulator and low flow needle valve at the rate of consumption by the combustion process. A high electric potential is placed across the two mesh planes using the output of a high voltage power amplifier capable of providing up to 10 kV (TREK model 609A), and ion currents are monitored using a Keithley 619 electrometer. As the voltage is increased from zero between the two gauze planes, the flame will deviate from its normal buoyant appearance to one of spherical symmetry, as in Fig. 3, and increasing the voltage further enters the negatively buoyant regime, where flame inversion occurs. A shadowgraph is used to visualize the point of balance. The visual indication of when the point of balance is reached is when the flame becomes spherically symmetric around the capillary, accompanied by an enlargement of the flame and a decrease in luminosity.

Previous experiments [1,3,8,9] have shown that if the ion saturation current is monitored as the voltage is increased, there is a plateau where, despite an increase in applied potential, an increase in current does not occur. This plateau corresponds to the microbuoyant condition for the $CH_4$-air flame in this geometry [3,8]. Therefore, we can use this plateau as a criterion for microbuoyancy for our flame. For these experiments, at a methane flow rate of 0.14 ml/s, the microbuoyant condition occurs at a mean field strength of approximately 422 V/cm. Once the microbuoyant condition has been reached pointwise measurements are made. CARS temperature measurements are taken, starting at the base of the flame horizontally outward in 1 mm intervals and downward in 1 mm intervals, totaling 14 mm horizontally and 12 mm vertically. For LIF, the measurements are made at 0.5 mm spacings up to 4 mm away from the flame to capture the high O2 concentration gradient in the region near the flame front, otherwise 1 mm spacings continue out to 8 mm horizontally and 10 mm vertically.

## 4. Coherent anti-stokes raman spectroscopy apparatus

A single shot coherent anti-stokes raman spectroscopy (CARS) instrument is used to take pointwise temperature measurements of $N_2$ in the capillary flame and its surroundings in a non-intrusive fashion. Descriptions of the CARS theory and practical implementation are given by Eckbreth [10] and Tolles et al. [11]. Figure 4 illustrates the layout of the CARS instrument. A broadband, modeless dye laser pumped by an Nd:YAG laser generates the Stokes beam using dual Bethune cells. The dye laser configuration and dye concentrations are used in a similar fashion to those described by Hahn et al. [12]. A Brewster window placed in front of the rear reflector is used to increase the beam power in the vertical polarization. A beam expander increases the size of the Stokes beam to maximize its overlap with the two pump beams when focused. The modeless dye laser is centered at the Stokes frequency $\omega_s$ (607.3 nm) and has a FWHM of approximately 6 nm. The frequency doubled 300 mJ NY61 to 10 Continuum YAG laser radiating at 532 nm is used to provide two pump beams $\omega_p$, as well as the input radiation to the dye laser. Thirty five percent of the laser energy is used directly for the CARS pump beams with the remainder pumping the dye laser. To avoid breakdown in the measurement control volume at room temperature, the energies of the beams entering the control volume are 30 mJ and 10 mJ for each pump beam and the Stokes beam, respectively.

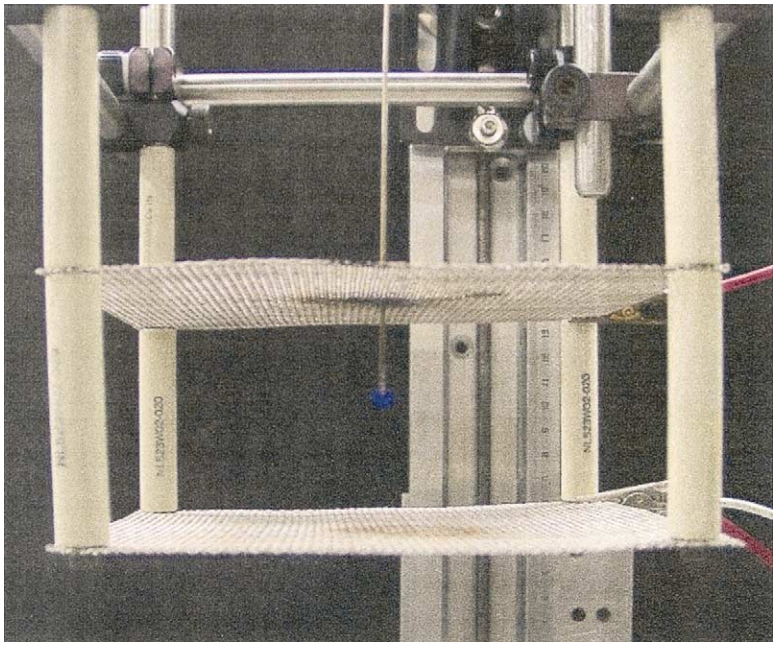

Fig. 2. Photograph of the electrically induced capillary flame apparatus.

CARS measurements in regions of large temperature gradients are spatially averaged and heavily biased toward the cold, high-density gas [13]. Since the capillary flame is on the order of 6 mm in diameter, we accept a reduction in signal strength to reduce the size of the sample volume to a point where spatial averaging can be considered small. Therefore, the CARS instrument used in these experiments is configured in a folded BOXCARS geometry with a Stokes half angle of 2.62° and 175 mm focal length lens, which provides a sample volume approximately 1 mm in length and 200 microns in diameter. CARS studies in flames with sizes similar to those of capillary flames show that spatial averaging occurs primarily along the longitude of the probe volume [14,15]; an effect that is reduced by orienting the largest dimension of the sample volume tangent to the isotherms.

A SPEX 1704 spectrometer ($f = 1$ m) fitted with a model 1420 EG&G OMA intensified camera is gated with a Princeton Instruments FG-100 pulser to directly record the CARS spectra. The polarization of the signal beam is rotated to maximize the diffraction efficiency of the spectrometer grating. Each measurement consists of approximately 50 CARS spectra and 50 background spectra. Each raw spectrum is divided by the modulation transfer function (MTF) of the detector to correct for the detector intensity nonlinearity, and is corrected for pixel spatial variations. The background noise is taken to be the average of the background spectra, and is subtracted from each signal spectrum. Each signal spectrum is then normalized by its integral to correct for laser shot-to-shot intensity variations, is averaged with the others, and the resulting spectrum is divided by the averaged non-resonant background spectrum. The non-resonant background spectrum is calculated from approximately 50 $CO_2$ spectra, corrected in the same fashion as the CARS signal. The resulting averaged CARS

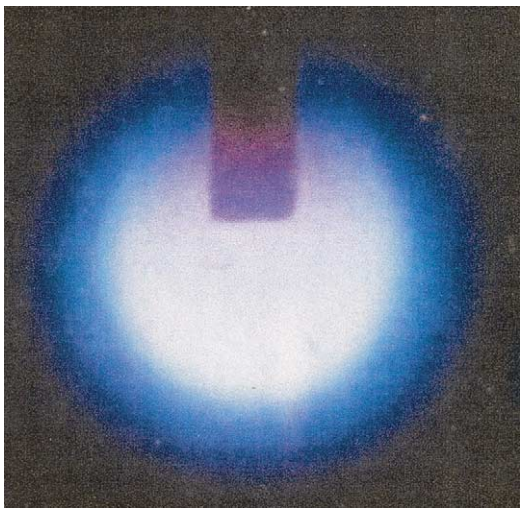

Fig. 3. Photograph of the capillary flame at the microbuoyant condition. The capillary is 1.7 mm in diameter for size scaling.

spectrum is compared to a theoretical spectrum generated by the CARSFIT code [16] convolved with the instrument (point-spread) function. CARSFIT uses a least squares fitting procedure to compare experimental data to the synthesized spectrum, and produces a $\chi^2$ value as the goodness of fit. The $\chi^2$ value is a sum of the squares of the difference between the data and theory at each point [17]. Values of $\chi^2$ below 1 are taken to be acceptable solutions and the corresponding spectra are further examined by eye and fitted manually if necessary. The instrument function is taken to be a combination of Gaussian and Lorentzian components [18]. Since the instrument function has been shown to be independent of temperature [19], it is found by varying the relative Gaussian-Lorentzian percentage, the Gaussian line width, and the Lorentzian line width until a good fit is achieved for a room temperature spectrum. A typical CARS spectrum is given in Fig. 5. This high temperature measurement is provided as an example of the quality of the fit even for a relatively low signal count.

## 5. Laser induced fluorescence apparatus

The experimental apparatus for laser induced fluorescence (LIF) detection is similar to that used in our past work [20–22], and is shown schematically in Fig. 6. A Lambda Physik LPX 210i ArF excimer laser emitting 20 ns pulses of 193 nm light excites oxygen molecules in the region outside of the capillary flame. The initial 1 cm by 3 cm beam is shaped by a 2.5 mm vertical slit and a 1 cm diameter iris aperture to minimize spatial averaging effects after focusing the beam. A 25 mm focal length, UV-grade lens focuses the beam to an area 0.7 mm wide and 100 microns tall, creating energy densities of 30 J/cm$^2$ per pulse. Isotropic emission from the sample volume is collected normal to the direction of laser propagation using a 5 cm diameter, 15 cm focal length lens, and is directed into a 0.3 m MacPhersen model 218 monochromator. The entrance and exit slit widths of the monochromator are 0.4 mm, providing a spectral resolution of 1.1 nm. A LeCroy Waverunner LT342 oscilloscope digitizes the signal from a Hamamatsu R928 photomultiplier tube attached to the monochromator for analysis. Measurements are taken at 0.22 nm intervals to capture the $O_2$ fluorescence spectrum between 200 nm and 300 nm at each condition. Each spectrum is presented as a 5 shot Savitsky-Golay rolling average. A representative $O_2$ spectrum taken of air at 925 K and atmospheric pressure is given in Fig. 7. Through calibration, both the 218 nm and 225 nm peaks were found to have nearly equal line strength dependencies; therefore,

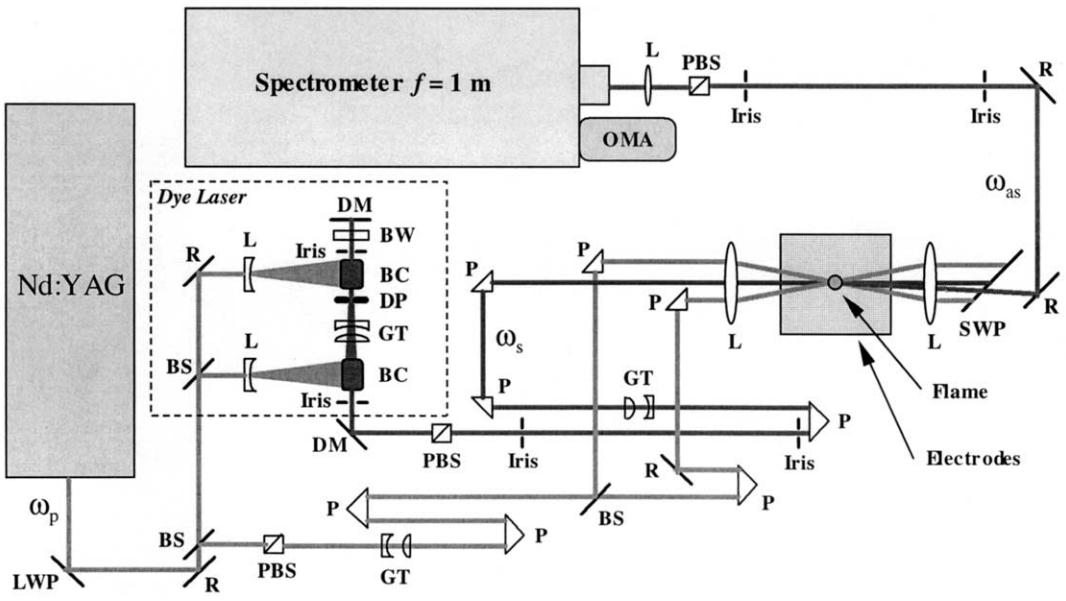


Fig. 4. CARS experiment layout. BS: dielectric beam splitter, BC: Buthane dye cell, BW: Brewster window, DP: diamond pinhole, GT: Gallilean telescope, HWP: half wave plate, L: plano-convex or cylindrical lens, LWP: long wave pass reflector, DM: Mirror, P: prism, PBS: polarizing beam splitter, SWP: short wave pass reflector, R: dielectric reflector, OMA: optical multi-channel analyzer, $\omega_s$: Stokes laser frequency, $\omega_{as}$: anti-Stokes laser frequency, $\omega_p$: pump laser frequency.

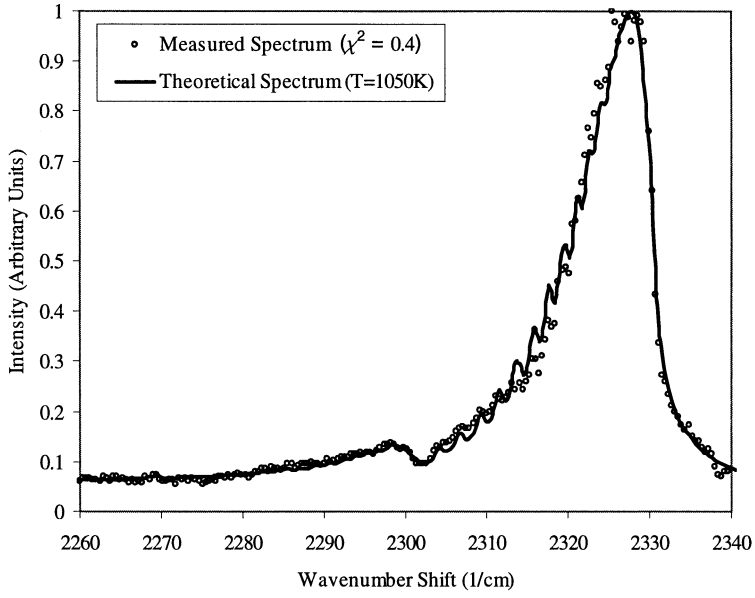


Fig. 5. A typical high temperature $N_2$ CARS spectrum. This figure provides a representative sample of the quality of fit for low signal counts. In this case, the $\chi^2$ goodness of fit index is 0.4.

only the peak at 218 nm is used to determine the $O_2$ concentrations.

LIF has been utilized by various researchers to make $O_2$ measurements of combustion systems. Detailed calculations of $O_2$ absorption and fluorescence in the Schumann-Runge bands excited by a 193 nm ArF laser between 300–2000 K indicate that the signal is highly dependent on temperature [23]. Andresen et al. [24] have shown that the quenching is negligible since $O_2$ is excited to a predissociative state, and they have developed the LIF technique for measuring $O_2$ in combustion flows. In general, the collected fluorescence signal ($S_f$) is given by,

$$S_f = E\, k\, N_{O2}\, L \left( \frac{A_{21}}{A_{21} + Q_q + Q_p} \right) \epsilon \left( \frac{\Omega}{4\pi} \right) \qquad (5)$$

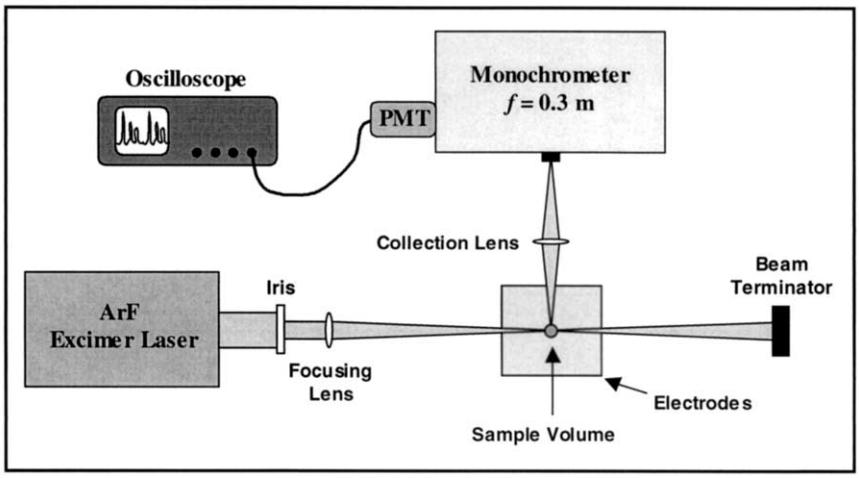


Fig. 6. LIF Experiment Layout. An ArF excimer laser produces 150 mJ, 20 NS pulses of 193 nm photons. This beam is shaped by an iris and focused to the laser interrogation region. Fluorescence is collected at a right angle to the incident beam and is focused into the monochromator. Signal transduced by the photomultiplier tube (PMT) is digitized by the oscilloscope and saved for analysis.

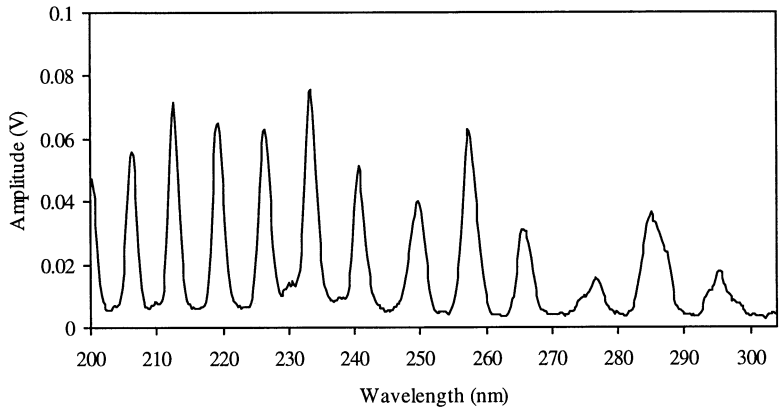


Fig. 7. Typical LIF $O_2$ Spectrum. This is a spectrum of 0.21 atm of $O_2$ at 925 K. The peak at 218 nm is used to determine the $O_2$ concentration.

where $E$ is the laser pulse energy, $k$ is the line strength for the transition, $N_{O2}$ is the number density of oxygen molecules, $L$ is the path length, $A_{21}/(A_{21}+Q_q+Q_p)$ is the Stern-Volmer fluorescence quantum yield, $\epsilon$ is the efficiency of the optics and the monochromator, and $\Omega/4\pi$ is the fraction of the isotropic emission collected.

The fluorescence quantum yield is the ratio of energy that is spontaneously emitted to the other modes of energy transfer. The $A_{21}$ is the Einstein spontaneous emission coefficient, $Q_q$ is collisional quenching term, and $Q_p$ is the loss of energy to the predissociative pathway. For $O_2$, the loss to predissociation dominates all other pathways, reducing the Stern-Volmer factor to $A_{21}/Q_p$, which is independent of temperature and pressure [23,24]. The terms $L$, $\epsilon$, $\Omega/4\pi$, and $A_{21}/Q_p$ are constant for all experimental conditions. The absorption of energy by $O_2$ in the beam path is calculated to be less than 2%, and, therefore, is negligible compared to the laser pulse energy. With these considerations accounted for, the collected fluorescence equation reduces to:

$$S_f = C_1 f(T)\, N_{O2} \tag{6}$$

where $C_1$ is a constant that includes $E$, $L$, $\epsilon$, $\Omega/4\pi$, and $A_{21}/Q_p$, and $f(T)$ is the temperature dependence of the line strength.

Molecular oxygen has many absorption bands in the 193 nm region and numerous discrete emission bands between 200 nm and 300 nm. To determine $f(T)$, a calibration is performed, measuring the emission at 218 nm as a function of temperature, as shown in Fig. 8. To do this, a 1 cm diameter Sylvania electric torch is used to heat the air from 400–1050

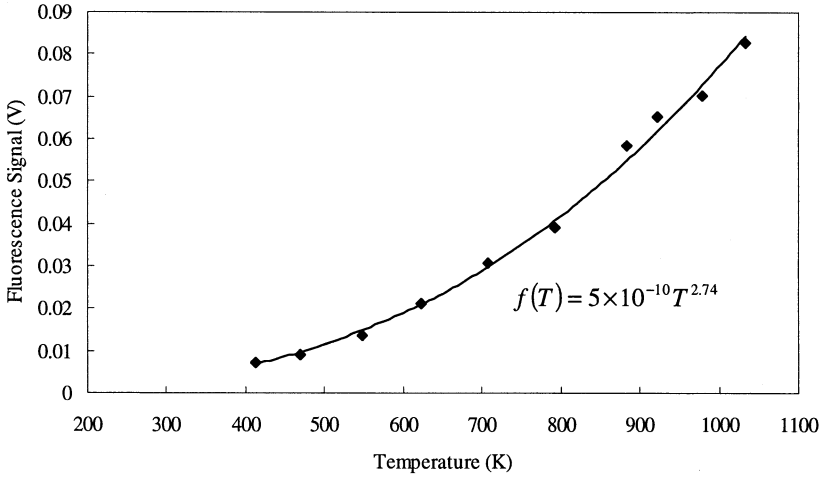


Fig. 8. Fluorescence signal dependence on temperature for $O_2$ in air.

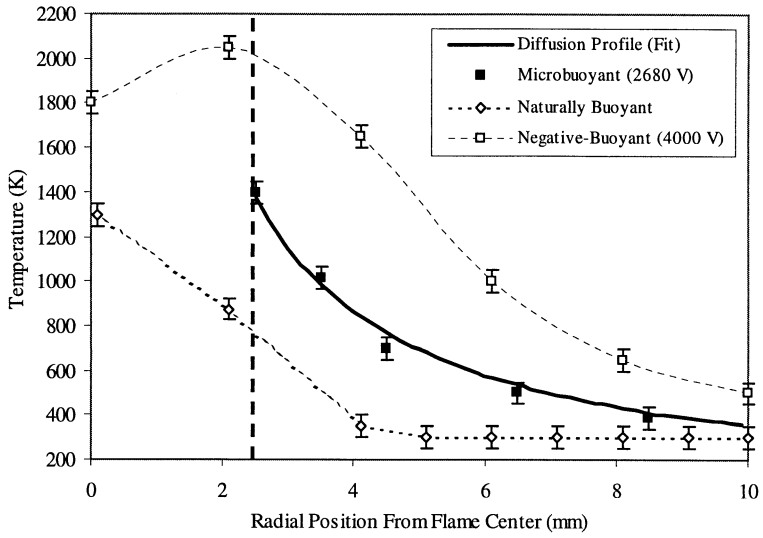


Fig. 9. Radial temperature profiles measured at 0 V, 2680 V, and 4000 V, corresponding to the naturally buoyant, microbuoyant, and negatively buoyant conditions. The dashed line represents the flame boundary at microbuoyancy, which is 2.5 mm from the flame center, as calculated from the coefficients obtained by fitting Eq. 6 to the measured curve.

K, and fluorescence measurements are taken at 10 points within this temperature range.

## 6. Results

### 6.1. Temperature and oxygen profiles at several g-loading conditions

A comparison between radial temperature profiles and $O_2$ concentration profiles taken directly below the flame for applied voltages corresponding to the naturally buoyant, microbuoyant, and negatively buoyant conditions is shown in Fig. 9. It has been shown [3] by the temperature profiles under these same conditions, together with shadowgraph images of the flame behavior, that a range of equivalent g-loadings on the flame is attainable by simply adjusting the voltage across the mesh planes.

Previous work [7,8], where both shadowgraph images and CARS measurements were employed, revealed that the shadowgraph image disappears near the bottom of the flame in the microbuoyancy condition, and CARS temperature measurements down the vertical axis of the flame obey a diffusion profile, corresponding to the flame structure predicted by theory in the absence of convection. That is,

$$T(r) = \frac{C_1}{r} + C_2 \tag{7}$$

where $r$ is the radial coordinate from the center of the flame. In this configuration, $C_1$ and $C_2$ are found through a two-parameter chi-squared fitting procedure. In Eq. 3, $C_1$ represents the flame radius multiplied by the maximum flame temperature, and $C_2$ represents the temperature infinitely far from the flame. Similarly, the $O_2$ concentration profiles can be fit to a diffusion profile of the form Eq. 8, corresponding to the flame structure described by Eq. 4. Comparing these two equations, $C_3$ is the oxidizer mass fraction at infinity (i.e. room air proportions).

$$Y_{OX}(r) = C_3 - \frac{C_4}{r} \tag{8}$$

Figures 9 and 10 show, respectively, the temperature and molecular oxygen concentration profiles for the naturally buoyant, microbuoyant, and negatively buoyant cases. In Fig. 9, the microbuoyant temperature profile is in good agreement with the theoretical profile within CARS measurement uncertainty, reaffirming previous findings [3]. For the naturally buoyant case, the temperature profile drops to room temperature over a shorter distance than in the microbuoyant case, as expected. This is a result of natural convective flows producing a stagnation point relatively close to the capillary tip, as implied by the shadowgraph images. Flame inversion is clearly evident in the negatively buoyant case. The electric field pulls the flame away from the capillary tube, thereby reducing the heat loss to the capillary, and producing a hot gas plume directed downward.

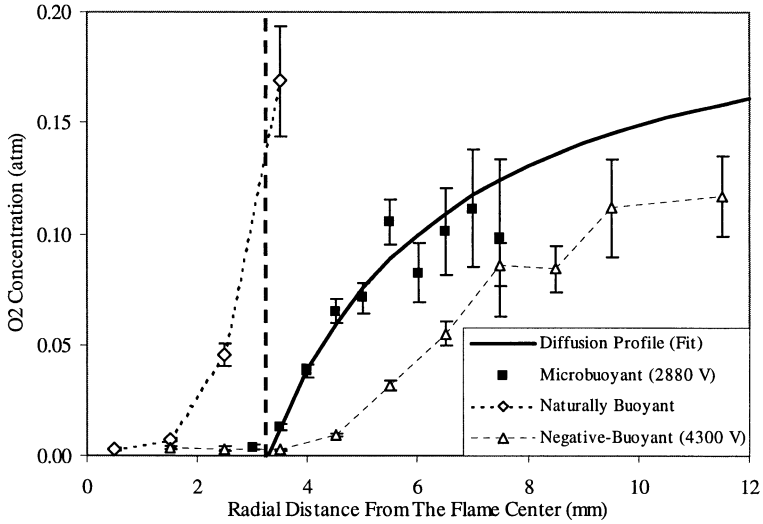


Fig. 10. $O_2$ concentration profiles measured at 0 V, 2880 V, and 4300 V, corresponding to the naturally buoyant, microbuoyant, and negatively buoyant conditions. The dashed line represents the flame boundary at microbuoyancy, which is 3.2 mm from the flame center, as calculated from the coefficients obtained by fitting Eq. 7 to the measured curve.

Therefore, the maximum temperature recorded at this condition is much higher, nearing the adiabatic flame temperature for $CH_4$-air combustion.

In Fig. 10, measured $O_2$ concentration profiles are plotted along with the theoretically derived profile, Eq. 8, for comparison. As with temperature, the microbuoyant profile matches the derived profile to 8 mm from the flame surface within the measurement uncertainty of the LIF system. Beyond this point, the measurement error increases as the distance from the flame increases because the fluorescence signal approaches the detection limit. Because the $O_2$ fluorescence depends on both the temperature and the $O_2$ concentration, the fluorescence signal decreases as the distance from the flame increases even though the $O_2$ concentration is increasing.

For the naturally buoyant case, the flame is drawn upwards by convective influences, which causes the flame front to move closer to the capillary. In this case, the concentration profile of $O_2$ is controlled by both diffusion and convection driven motion. As a result, the concentration gradient is steeper and the $O_2$ partial pressure approaches 0.21 atm faster than in the microbuoyant case. Conversely, in the negatively buoyant case, the flame is pulled downward. Figure 10 shows low molecular oxygen concentrations extending downward 6 mm from the end of the capillary, reflecting a downward plume of combustion products; the $O_2$ concentration increases, but less steeply than in the other cases.

### 6.2. Flame radius calculation

The flame radius can be calculated analytically using the mixture fraction method [6]. This is used to check if both the temperature and $O_2$ concentration measurements return values that are consistent. Eq. (9) reflects the position where the fuel and oxidizer meet at stoichiometric proportions, thereby defining the flame radius,

$$r_f = Z\dot{m}_f \ln\left(\frac{\nu + 1}{\nu}\right) \tag{9}$$

where $\nu$ is the stoichiometric coefficient by mass for $CH_4$-air combustion ($\nu = 17.16$), and Z is the Zeldovich parameter described earlier.

For low flow rates, the flame radius is most easily determined from the oxidizer fit equation. By equating the coefficients from Eq. 4 and Eq. 8, through $C_3$, the equation for the flame radius is given as,

$$r_{f,\exp} = Z\dot{m}_f \ln\left(1 + \frac{1}{C_3}\right) \tag{10}$$

Using the chi-squared fitting procedure, the coefficients $C_1$, $C_2$, $C_3$, and $C_4$ in Eq. 7 and Eq. 8 are found to be 3416 K · cm, 11 K, 0.2216 atm, and 0.7294 atm · mm, respectively. Using the fitting parameter, the flame radius if found through $C_1$ by dividing out the maximum temperature measured at the microbuoyant condition, and by examining the point at which the $O_2$ concentration goes to zero. The

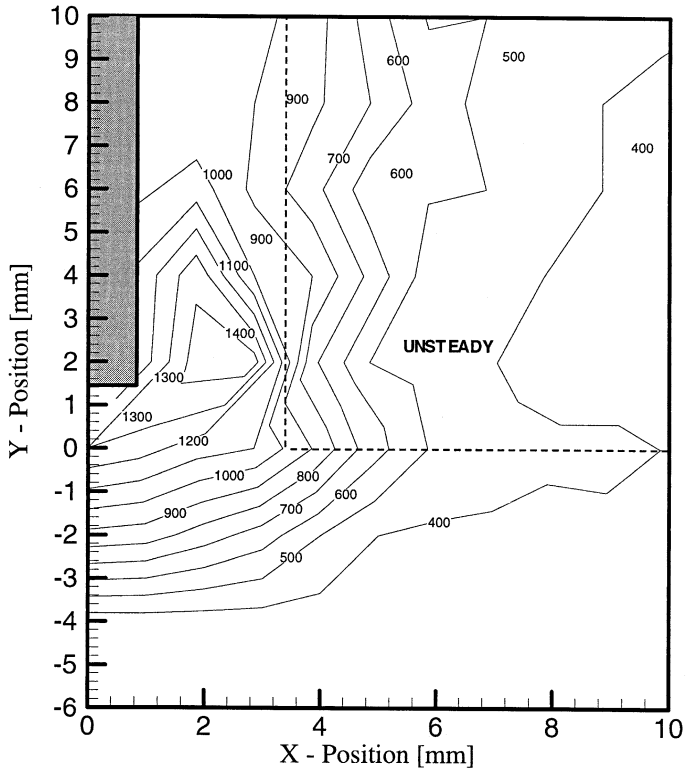


Fig. 11. 2-D temperature profile of the capillary flame with no applied voltage (naturally buoyant condition). The close proximity of the isotherms directly below the capillary indicates a high temperature gradient. A high temperature exhaust plume is moving up the outside of the capillary. Dashed lines are drawn to indicate regions of time-averaged temperatures.

resulting flame radii calculated from the temperature and oxidizer fits are 2.5 mm and 3.2 mm, respectively. These values correspond well with the flame radius obtained visually from Fig. 2, which is approximately 3 mm.

Once the flame radius is obtained, analytically solving for the Zeldovich parameter gives us a value for $\rho$D used in the unity Lewis number approximation. Therefore, we can obtain the equivalent temperature at which the approximation holds the diffusion coefficient constant. Through Eq. 3 and Eq. 4 and by choosing $r_f = 3.2$ mm, the Zeldovich parameter, Z = 2044 mm · s/kg, which reflects a $\rho$D value associated with a temperature near 550 K.

### *6.3. Temperature field measurements*

Point-by-point CARS temperature measurements taken in the grid pattern described earlier are used to obtain contour maps of the region directly below the flame. Figures 11 to 13 illustrate these pointwise temperature field measurements, corresponding to the naturally buoyant microbuoyant, and negatively buoyant situations, respectively. The contour plot for each case is generated by interpolating values between the measured points using TECPLOT. In all cases, the origin is taken to be the position of the center of the spherical flame at microbuoyancy, as estimated from the photograph in Fig. 3 using the capillary diameter as the length scale; the capillary tip is 0.4 mm above the origin. The flame provides a measurement boundary in the microbuoyant case, in which a lack of $N_2$ and $O_2$ prevents CARS and LIF signals from being generated. The presence of convection in both the naturally buoyant and negatively buoyant situations, however, allows air to penetrate into the flame zone, making it possible to measure inside the flame.

Convection, drawing the exhaust gases upward in the naturally buoyant case, is clearly illustrated in Fig. 11 by the close proximity of the isotherms below the capillary tip and high temperatures that extend upward along the capillary wall. The buoyant flow moving upward entrains colder gas, resulting in fluctuating CARS measurements. The resulting temperatures shown in this region of the figure reflect time-averaged values in this unstable region. Therefore, the uncertainty in these areas is very high. Dashed

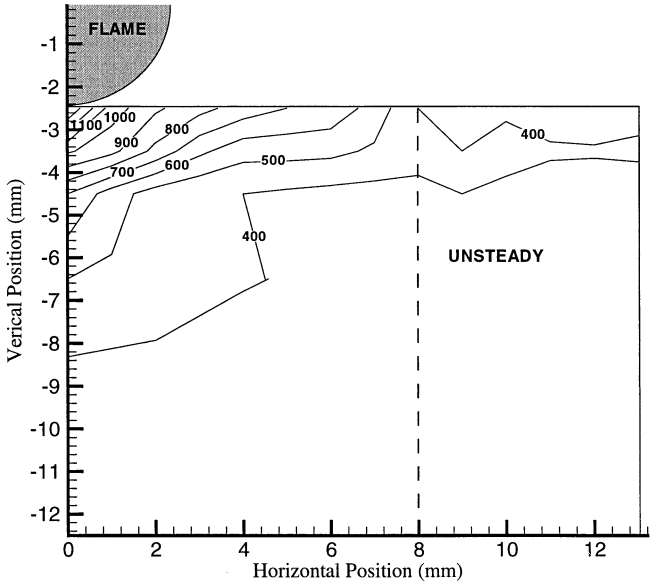


Fig. 12. 2-D temperature profile of the electrically induced microbuoyant flame. A voltage of approximately 2680 V is applied across the 6.35 cm (2.5 in) gap. The dashed line is drawn to indicate the region approximately 8 mm from the longitudinal axis of the capillary where a thermal gradient exists, outside of which the measured temperatures are unsteady. The reported temperatures in this region reflect a time-average.

lines are drawn in to isolate this region from the rest of the figure.

The temperature field measured at the microbuoyant condition, given in Fig. 12, illustrates nearly symmetric thermal gradients in the region below the flame. Previous work [3], where shadowgraph images were employed suggested there is a distinct temperature gradient in the microbuoyant condition

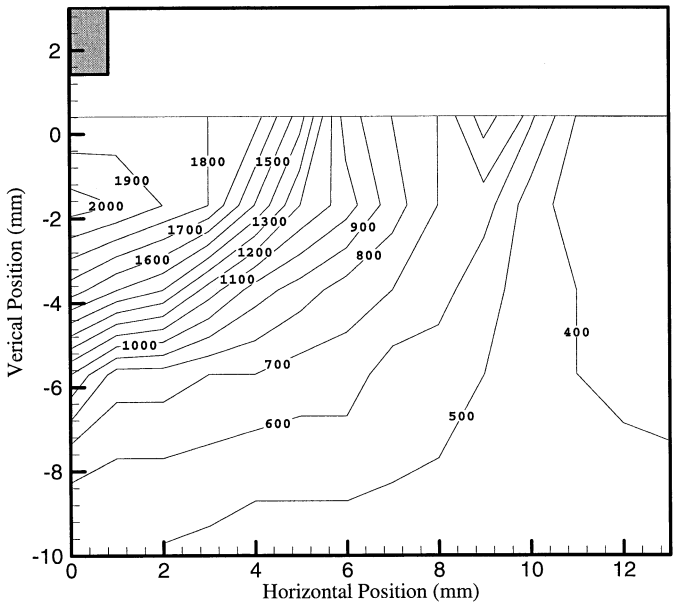


Fig. 13. 2-D temperature profile of the capillary flame in a representative negatively buoyant condition. A voltage of approximately 4000 V is applied across a 6.35 cm (2.5 in) gap. High temperatures extend downward much farther than in the other two situations, indicating an exhaust plume directed downward.

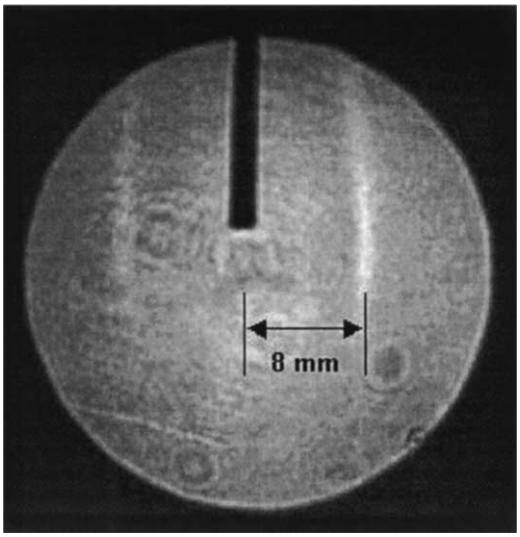


Fig. 14. Shadowgraph image complements of Strayer et al. [3]. The region approximately 8 mm from the longitudinal axis of the capillary indicates a thermal gradient exists at this point.

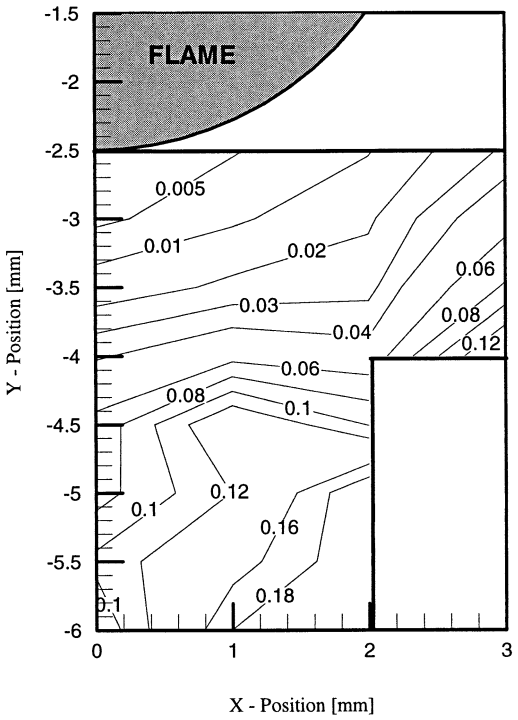


Fig. 15. 2-D $O_2$ concentration profile of the capillary flame at microbuoyancy. The applied voltage is roughly 2880 V across a 6.35 cm (2.5 in) gap.

approximately 8 mm from the vertical axis of the flame (see Fig. 14). CARS measurements taken out toward this region fluctuate considerably, reinforcing this observation. These measurements are indicative of convective flow outside of this region, and provide a physical boundary that prevents complete spherical symmetry.

A representative negatively buoyant case is given in Fig. 13, when 4000 V is applied to the system. Flame inversion occurs visibly by eye, the temperature is elevated much further below the flame, and the maximum temperature measured approaches $CH_4$-air adiabatic combustion temperature. The isotherms spread out indicating a decrease in the thermal gradient below the capillary. Spreading of the hot products, similar to a jet of hot gas entering a colder medium, indicates a downward convection of exhaust products resulting from negative g-loading on the flame.

### *6.4. $O_2$ concentration field measurements*

The resulting $O_2$ concentration profile, taken at the microbuoyant condition, is given in Fig. 15. As with temperature, the values between the pointwise measurements are interpolated to obtain a contour map. As noted earlier, LIF points are taken in a 0.5 mm by 0.5 mm grid pattern throughout the 4 mm by 4 mm region starting at the origin, and the spacing is increased to 1 mm by 1 mm beyond. The uncertainty in LIF concentrations is increased because they carry both the uncertainties from the LIF apparatus and CARS measurements. Consequently, LIF concentrations and uncertainties are calculated using CARS temperatures. The measurements that include uncertainties less than 25% are reported in this figure.

This figure shows that the $O_2$ concentrations exhibit spherical symmetry in the region near the vertical radius. However, this profile increasingly steepens with increasing angle from the vertical. Physically, this may have three explanations: 1) the turbulent region 8 mm from the longitudinal axis incurs mixing between static gas (held by the ion wind) and the buoyant flow outside this region (implied to exist by the density gradients in the shadowgraph, and by fluctuating CARS temperatures); 2) spherical symmetry does exist in a larger region than depicted due to high measurement uncertainty; or 3) the flame experiences a negative buoyancy due to being slightly overdriven by the electric field.

### *6.5. Determining the extent of microbuoyancy*

In order for the laboratory microbuoyant flame to represent that of a microbuoyant flame burning in zero gravity, both the temperature and oxidizer pro-

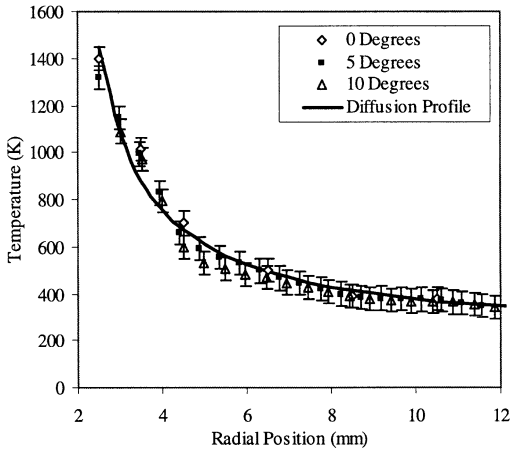


Fig. 16. Radial temperature profiles of an electrically induced microbuoyant flame taken at 0, 5, and 10 degrees from the vertical axis. These curves represent the microbuoyancy condition within experimental uncertainty.

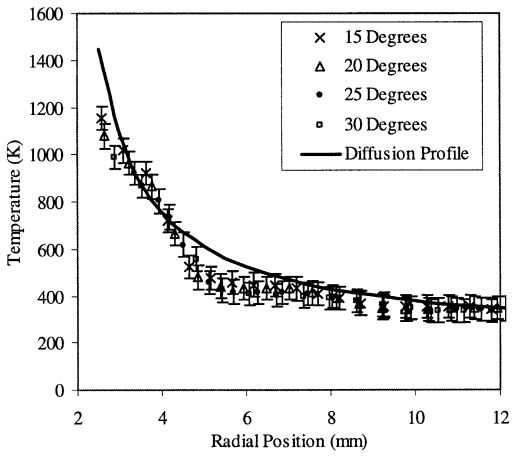


Fig. 17. Radial temperature profiles of an electrically induced microbuoyant flame taken at 15, 20, 25, and 30 degrees from the vertical axis. The gradients depart too far from theory for this region to be considered microbuoyant.

files must demonstrate symmetry and diffusive character within measurement error. The challenge of taking measurements in an environment such as this one is due to the small scale of the flame and large gradients that exist within it. Therefore, the uncertainties in the CARS measurements are determined by varying the temperature used to synthesize the theoretical spectrum and comparing spectra. The resulting error is nearly constant with temperature (approximately $\pm$ 50K everywhere except in unstable regions); hence, the high temperature region yields lower percentage error. For LIF measurements, the uncertainty is calculated in the standard way [25]. However, since the CARS temperature measurements are required to calculate $O_2$ concentrations, LIF uncertainties become very large as the temperature decreases. Thus, the extent of microbuoyancy is obtained essentially through the temperature profiles.

Earlier, measurements taken along the vertical radius of the flame extending downward were fit to the theoretical diffusion profile. Radial lines are drawn through the interpolated field at 5° intervals, and compared to the theoretical temperature profile up to 30° from the vertical axis. Figure 16 shows radial curves taken at 0°, 5°, and 10° from the vertical axis. These curves adequately follow a theoretical diffusion profile, and represent microbuoyancy within the accuracy of the CARS measurements. Beyond 10°, however, the temperature gradient increases beyond that expected from Eq. (3) in the region closest to the flame. Figure 17 illustrates that radial curves taken beyond 10 degrees depart from the theoretical profile beyond measurement uncertainty. As implied by shadowgraph images, sharp thermal gradients disappear in the region directly below the flame, but begin to appear with increasing angle from the vertical axis. In this configuration, the result is a wedge-shaped region that exhibits microbuoyant behavior. Using the error associated with the CARS temperature measurements in this experiment as a maximum error between theoretical and experimental curves, the azimuthally symmetric region of the flame extends 10° from the longitudinal axis.

## 7. Conclusions

In the current study, both CARS temperature measurements and LIF $O_2$ concentration measurements are taken of an electrically induced microbuoyant flame. Temperature and $O_2$ concentration profiles are taken along the radial line extending directly below the flame at three voltage conditions that correspond to a naturally buoyant, microbuoyant and negatively buoyant flame. The results show that both profiles in each condition vary considerably from the other two conditions, strengthening the propositions that an effectively zero-gravity burning situation can exist in the laboratory, and that a fairly wide range of effective g-loadings can be applied in an Earth-based laboratory experiment. Measurements taken of the naturally buoyant flame are consistent with what is observed in the laboratory. For example, the distance between the flame and the capillary tip decreases, and the temperature and $O_2$ concentration gradients below the flame steepen, as compared to the microbuoyant and negatively buoyant cases. Measured temperatures and $O_2$ concentrations in the micro-

buoyant case fit well to theoretical profiles corresponding to spherically symmetric flame structure in the absence of convection. In the negatively buoyant case, both temperature and $O_2$ concentration gradients decrease below the flame, and the flame stands further from the capillary tip. A thermal plume extending downward creates high temperatures far from the flame, and the $O_2$ profiles reach ambient conditions further out as well.

These experiments show that directly below the electrically balanced microbuoyant flame the temperature profile has the diffusive character expected in a spherically symmetric combustion situation. The extent of this symmetry is determined by examining the temperature field measured at the microbuoyant condition, which shows that a section of electrically induced microbuoyancy extends approximately 10° from the longitudinal axis of the capillary flame. Whether this extent is sufficient for simulating microgravity combustion depends on the physical processes being explored and how much of the flame participates in them.

## Acknowledgments

The authors gratefully acknowledge discussions with Professor Felix Weinberg of Imperial College regarding his extensive theoretical and experimental work in the concepts of this research, and Dr. Ben Strayer and Dr. Jonathan Posner for many helpful discussions on experimental results and the CARS system. We also thank Professor Ron Hanson of Stanford University for lending the Sylvania air heater. This work is supported by NASA under contract NAG3-2226 and by the Environmental Health Sciences Superfund Basic Research Program (Grant Number P42 ESO 47050-01) from the National Institute of Environmental Health Sciences.

## References

[1] J. Lawton, F.J. Weinberg, Electrical Aspects of Combustion, Clarendon Press, Oxford, 1969.
[2] F.B. Carleton, F.J. Weinberg, Joint meeting of the Portuguese, British, Spanish, and Swedish Sections of The Comb. Inst., April 1-4, Madeira, 1996, p. 8.
[3] B.A. Strayer, J.D. Posner, D. Dunn-Rankin, F.J. Weinberg, Proc. Royal Soc. A. 458 (2002) 1151.
[4] D.B. Spalding, Fourth Symposium (International) on Combustion, The Combustion Institute, Pittsburgh (1953) 846.
[5] G.A.E. Godsave, Fourth Symposium (International) on Combustion, The Combustion Institute, Pittsburgh (1953) 818.
[6] S.R. Turns, An Introduction to Combustion Concepts and Applications, 2nd ed., McGraw-Hill, 2000.
[7] M.Y. Choi, F.L. Dryer, in: Microgravity Combustion: Fire in Free Fall, H.D. Ross (Ed.), Academic Press, 2001.
[8] K. Gugan, J. Lawton, F.J. Weinberg, Tenth Symposium (International) on Combustion, The Combustion Institute, Pittsburgh, (1965) 709.
[9] B.A. Strayer, J.D. Posner, D. Dunn-Rankin, Spring Meeting, Western States Section/The Comb. Inst., Golden CO, 13th March, 2000.
[10] A.C. Eckbreth, Laser Diagnostics for Combustion Temperature and Species, Abacus Press, Cambridge, 1988.
[11] W.M. Tolles, J.W. Nibler, J.R. McDonald, A.B. Harvey, Appl. Spec. 31 (4) (1977) 253.
[12] J.W. Hahn, C.W. Park, S.N. Park, Appl. Opt. 36 (1997) 6722.
[13] J. Garman, D. Dunn-Rankin, Combust. Flame 115 (1998) 481.
[14] J.Y. Zhu, D. Dunn-Rankin, Appl. Opt. 30 (1991) 2672.
[15] J.Y. Zhu, D. Dunn-Rankin, Appl. Phys. 56 (1993) 47.
[16] G. Clark, “The CARSFIT Code” Version 7-24-01, 2001.
[17] W.H. Press, S.A. Teukolsky, W.T. Vetterling, B.P. Flannery, Numerical Recipes in Fortran 77, 2nd ed., Cambridge University Press, Cambridge, U.K. (1992) 653.
[18] R.P. Lucht, R.E. Teets, R.M. Green, R.E. Palmer, C.R. Ferguson, Combust. Sci. Technol. 55 (1987) 41.
[19] D.R. Snelling, R.A. Sawchuck, G.J. Smallwood, T. Parameswaran, Rev. Scientific Instruments 63 (12) (1992) 5556.
[20] C.B. Stipe, B.S. Higgins, D. Lucas, R.F. Sawyer, C.P. Koshland, Western States Section/The Comb. Inst., Salt Lake City, UT, 15th October, 2001.
[21] C.S. McEnally, C.P. Koshland, D. Lucas, R.F. Sawyer, Applied Optics 33 (1994) 3977.
[22] S.G. Buckley, C.S. McEnally, R.F. Sawyer, C.P. Koshland, D. Lucas, Combustion Science and Technology 118 (1996) 169.
[23] M.P. Lee, R.K. Hanson, Quant. Spectrosc. Radiat. Transfer 36 (5) (1986) 425.
[24] P. Andresen, G. Meijer, H. Schlüter, H. Voges, W. Koch, W. Hentschel, W. Opperman, E. Rothe, Applied Optics 29 (16) (1990) 2392.
[25] J.R. Taylor, An Introduction to Error Analysis, University Science Books, 1982.